

Spatial Dynamics of DNA Damage Response Protein Foci along the Ion Trajectory of High-LET Particles

Author(s): Guanghua Du, Guido A. Drexler, Werner Friedland, Christoph Greubel, Volker Hable, Reiner Krücken, Alexandra Kugler, Laura Tonelli, Anna A. Friedl and Günther Dollinger

Source: Radiation Research, 176(6):706-715.

Published By: Radiation Research Society

DOI: <http://dx.doi.org/10.1667/RR2592.1>

URL: <http://www.bioone.org/doi/full/10.1667/RR2592.1>

BioOne (www.bioone.org) is a nonprofit, online aggregation of core research in the biological, ecological, and environmental sciences. BioOne provides a sustainable online platform for over 170 journals and books published by nonprofit societies, associations, museums, institutions, and presses.

Your use of this PDF, the BioOne Web site, and all posted and associated content indicates your acceptance of BioOne's Terms of Use, available at www.bioone.org/page/terms_of_use.

Usage of BioOne content is strictly limited to personal, educational, and non-commercial use. Commercial inquiries or rights and permissions requests should be directed to the individual publisher as copyright holder.

Spatial Dynamics of DNA Damage Response Protein Foci along the Ion Trajectory of High-LET Particles

Guanghua Du,^{a,b,1} Guido A. Drexler,^c Werner Friedland,^d Christoph Greubel,^e Volker Hable,^e Reiner Krücken,^a Alexandra Kugler,^c Laura Tonelli,^a Anna A. Friedl^{c,2} and Günther Dollinger^{e,1,2}

^a Physik Department E12, Technische Universität München, 85748, Garching, Germany; ^b Institute of Modern Physics, Lanzhou, Gansu Prov. 730000, P. R. China; ^c Department of Radiation Oncology, Ludwig-Maximilians-Universität München, 80336 Munich, Germany; ^d Institute of Radiation Protection, Helmholtz Zentrum München, 85764 Neuherberg, Germany; and ^e Angewandte Physik und Messtechnik, LRT 2, Universität der Bundeswehr München, 85579, Neubiberg, Germany

Du, G., Drexler, G. A., Friedland, W., Greubel, C., Hable, V., Krücken, R., Kugler, A., Tonelli, L., Friedl, A. A. and Dollinger, G. Spatial Dynamics of DNA Damage Response Protein Foci along the Ion Trajectory of High-LET Particles. *Radiat. Res.* 176, 706–715 (2011).

High-linear energy transfer (LET) ion irradiation of cell nuclei induces complex and severe DNA lesions, and foci of repair proteins are formed densely along the ion trajectory. To efficiently discriminate the densely distributed/overlapping foci along the ion trajectory, a focus recognition algorithm called FociPicker3D based on a local fraction thresholding technique was developed. We analyzed high-resolution 3D immunofluorescence microscopic focus images and obtained the kinetics and spatial development of γ -H2AX, 53BP1 and phospho-NBS1 foci in BJ1-hTERT cells irradiated with 55 MeV carbon ions and compared the results with the dynamics of double-strand break (DSB) distributions simulated using the PARTRAC model. Clusters consisting of several foci were observed along the ion trajectory after irradiation. The spatial dynamics of the protein foci supports that the foci clusters are not formed by neighboring foci but instead originate from the DSB cluster damage induced by high-LET radiations. © 2011 by Radiation Research Society

INTRODUCTION

Many DNA damage response and repair proteins form immunofluorescence foci at the sites of DSBs in cells after exposure to ionizing radiation, such as γ -H2AX (phosphorylated histone H2AX), phospho-NBS1 (serine-343) and 53BP1 (1–4). Focus scoring has proven to be a sensitive method in the study of the kinetics of DNA damage response and DNA repair after ionizing

radiation. The microscopic images of immunofluorescent foci provide the protein information at sites of DSBs even at doses as low as several centigrays (5, 6). The ionizing radiation-induced foci (IRIF) that occur after exposure to low-LET ionizing radiations like X rays, γ rays and electron beams are distributed randomly in the cell nucleus; after high-LET ion irradiation, the IRIF are distributed densely along the ion trajectory (7).

The individual foci formed after high-LET ion irradiation are difficult to analyze because they are located very close to each other along the ion trajectory. Most of the previous studies on protein focus kinetics after high-LET irradiation were not based on measurements of individual foci, because the foci induced by one ion traversal are resolved as a single focus in the case of the perpendicular irradiation geometry and 2D microscopy, and even if 3D microscopy is used, individual foci are difficult to discriminate due to the axial resolution limit of the microscopy (8–12). Jakob *et al.* have demonstrated that individual foci formed along the trajectory after high-LET ion irradiation can be distinguished when the cell monolayer is irradiated with a small angle to the direction of the energetic ions (13). Using this kind of radiation, Aten *et al.* later reported that focus clusters are formed along the ion trajectory in cells irradiated with high-LET α particles (14). It is still not fully understood how the focus clusters are formed.

Even with small-angle irradiation, the study of individual foci along the ion trajectory cannot be performed accurately, because the densely distributed and overlapping foci along the ion trajectory cannot be efficiently discriminated by current available focus recognition software.

In this work, we introduce a new algorithm called FociPicker3D for the discrimination and spatial analysis of densely distributed and overlapping objects. We demonstrate its application to the study of spatial kinetics of high-LET radiation-induced foci in human fibroblast cells within several hours after carbon-ion irradiation.

¹ Addresses for correspondence: Institute of Modern Physics, CAS, Nanchan Road 509, Lanzhou, Gansu Prov. 730000, China; e-mail: gh_du@impcas.ac.cn; Universität der Bundeswehr München, Institute for Applied Physics and Metrology, Werner-Heisenberg-Weg 33, Neubiberg, Bavaria 85577, Germany; e-mail: guenther.dollinger@unibw.de.

² Joint senior authorship.

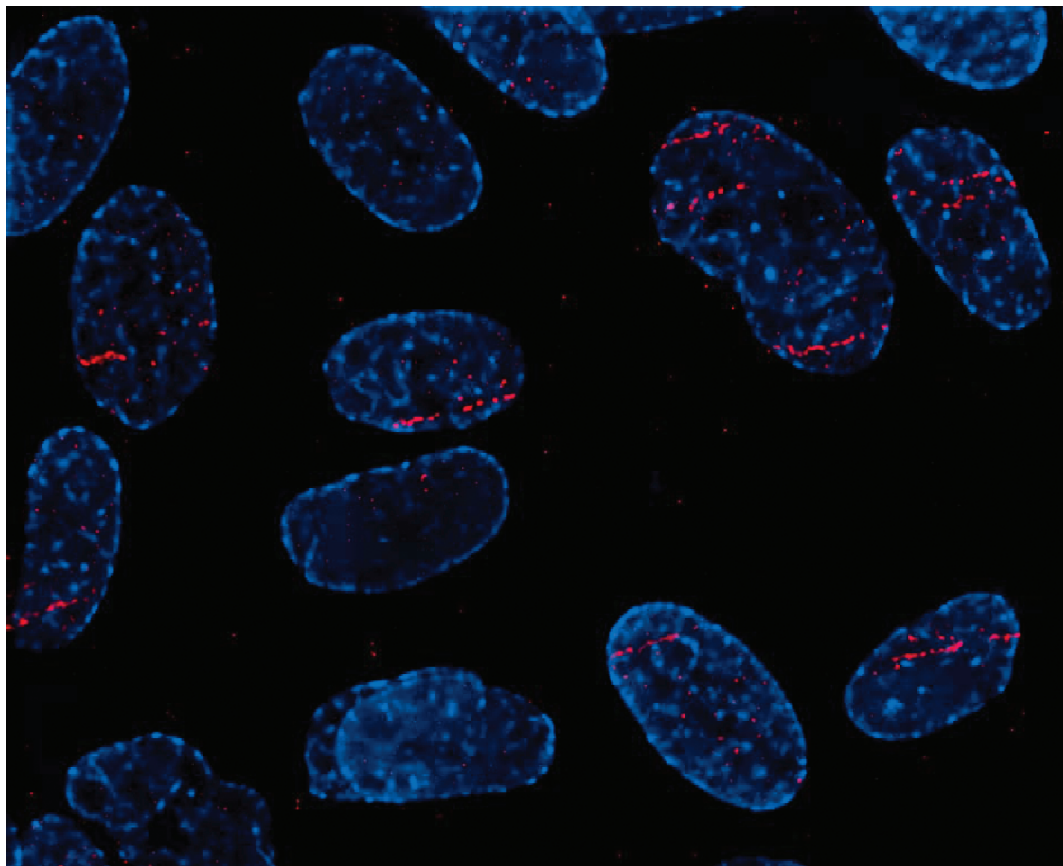


FIG. 1. Microscope image of γ -H2AX focus streaks in BJ1-hTERT cells after 55 MeV carbon-ion irradiation with a 10° small angle to the cell monolayer. The cells were fixed 3 min after irradiation, immunostained with γ -H2AX antibodies (red), and counterstained with DAPI (blue). Each red focus streak indicates a carbon-ion traversal. The image represents the maximum projection of 22 slices of the deconvoluted 3D microscopic image.

The obtained kinetics of the foci is compared to the simulated DSB kinetics based on a theoretical model using the PARTRAC code (15). Finally, we propose a model to explain the formation of focus clusters.

MATERIALS AND METHODS

Cell Culture, Irradiation and Immunofluorescence Microscopy

BJ1-hTERT cells (BD Clonotech, Germany) were cultured in a medium mixture of Dulbecco's modified Eagle's medium (DMEM) and medium 199 (catalog nos. D6429 and M4530, Sigma-Aldrich) supplemented with 10% fetal calf serum (FCS) and 1% penicillin-streptomycin solution (10k U penicillin, 10 mg streptomycin/ml). HeLa cells were cultured in RPMI 1640 medium (PAA-Laboratories, Austria) supplemented with 10% FCS plus L-glutamine and 1% penicillin-streptomycin solution. All cells were incubated at 37°C (100% humidity, 95% air + 5% CO_2).

The cells were seeded into cell dishes made of a stainless steel ring with a culture bottom of 6- μm -thick Mylar foil pretreated with Cell-TAK (BD Bioscience) 24 h before irradiation. Then the cells were irradiated with 55 MeV carbon ions (LET = 380 keV/ μm as they enter the cell monolayer; the average dose per ion traversal is 0.79 Gy) at the Munich microprobe SNAKE [Superconducting Nanoprobe for Applied nuclear (Kern-) physics Experiments] (16). The carbon-ion beam hit the cells at an angle of 10° with respect to the cell monolayer. For X irradiation, cells were exposed to 1 Gy of 250 kV X rays. After

the irradiation, the cells were further incubated at 37°C and then fixed after different incubation times. For focus analysis, the cells were immunostained with mouse γ -H2AX (catalog no. 05-636, Upstate, 1:350), mouse 53BP1 (catalog no. 05-726, lot 24568, Upstate, 1:400) or rabbit phospho-NBS1 (serine-343) (catalog no. NB100-284, Novus Biologicals, 1:500) antibodies at 3, 15, 45, 120 and 360 min after carbon-ion irradiation. To obtain the detailed structure of the focus streak, high-resolution 3D microscopy was performed. The immunofluorescence image stacks (slice distance 0.25 μm , 20–40 slices per stack, 12 bit) were acquired with an inverse epifluorescence microscope (Zeiss Axioobserver Z1) using a Zeiss Plan Apocromat 63 \times objective [glycerol immersion, numeric aperture (NA) 1.4]. The wide-field microscopic images were deconvoluted using the classical maximum likelihood estimation (CMLE) algorithm (Huygens Software, the Netherlands). The immunostaining procedure has been described in detail previously (17).

Image Processing and Analysis

The 55 MeV carbon ions generate a dense track of ionizations in cells, which consequently results in dense DNA damage. Closely distributed protein foci formed at DSB sites along the ion trajectories become visible, as shown in Fig. 1. A 2D region of interest (ROI) covering only the focus streak was chosen manually to exclude spontaneous foci outside of the streak plane. Then these ROIs (foci as shown in Fig. 2A and Fig. 3a) were stored in separate images and the images were normalized to 8 bit (maximum 255) according to the maximum pixel value in the focus streak using a home-made 8 bit

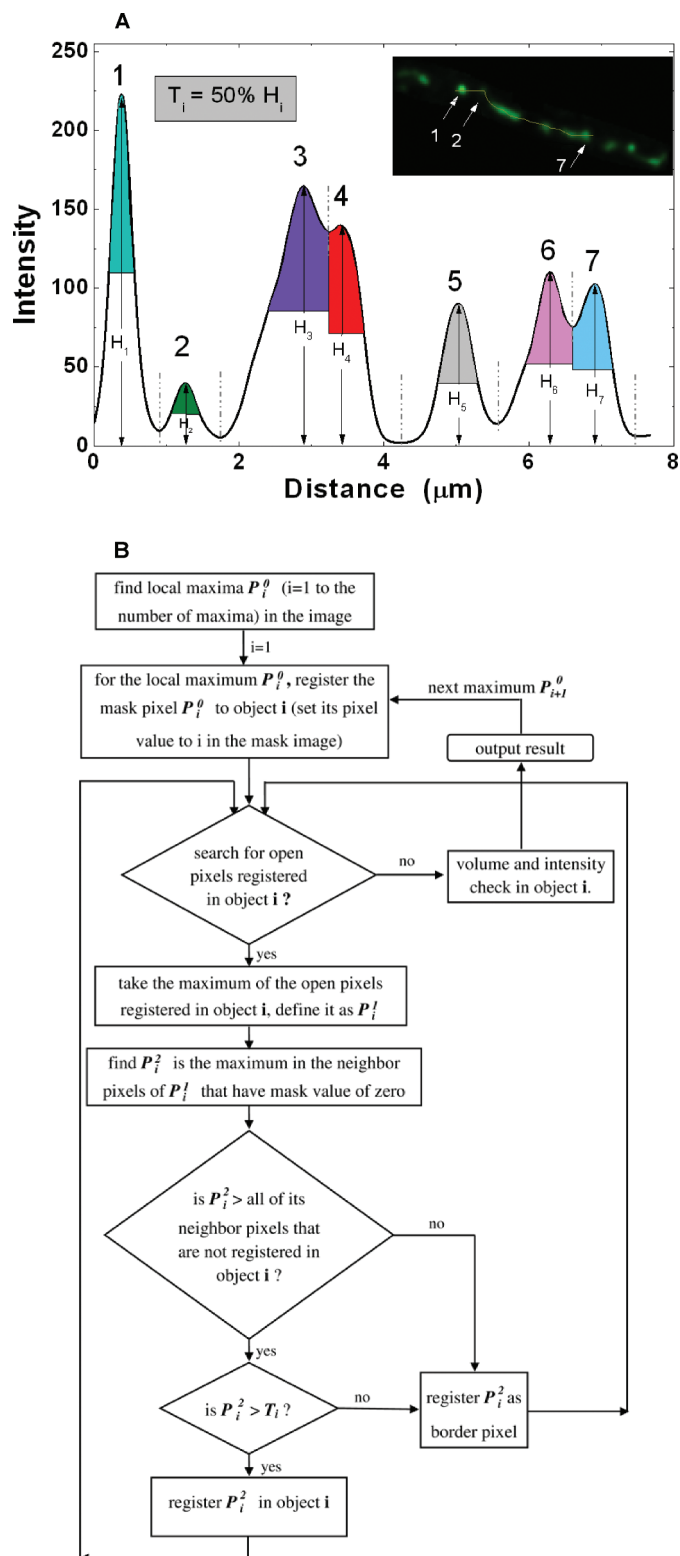


FIG. 2. Panel A: The principle of the FociPicker3D algorithm illustrated using a 1D intensity profile. The inset shows the microscopic image of a 53BP1 streak of a carbon-ion-irradiated BJ1-hTERT cell (max-projection). The plot represents the intensity profile of the line over the foci as illustrated in the streak image. The objects are defined at the local maxima and then segmented (drawn in colors) by the fraction threshold T_i and the minima. Panel B: The workflow of the FociPicker3D algorithm.

converter (tests showed that similar focus numbers were obtained from 12-bit images and 8-bit images; data not shown). Then these streak images were analyzed by the FociPicker3D program described below to obtain spatial information for the foci along the carbon-ion trajectory (with fraction threshold setting $F = 20\%$, minimum focus volume = 20 pixels).

The focus discrimination of the FociPicker3D algorithm was compared to the thresholding method using the 3D Object Counter (18) and the top-hat filter TopHatFilter3D (19) with optimal parameter settings, i.e. those that gave the best focus recognition.

Measurement of Focus Volume

The FociPicker3D plug-in enables us to measure the volume of the protein foci quantitatively using immunofluorescence image stacks of the irradiated cells. However, due to the different resolution in X and Y vs. Z dimensions in wide-field microscopy, the foci have an elongated ellipsoid shape in Z. Especially when the focus size is below the Z-resolution, the focus depth in Z is significantly influenced and becomes larger than its actual size due to the blur in Z. To correct this and to obtain the accurate Z-depth of the foci, we projected the 3D focus mask onto the XY, XZ and YZ planes and measured their areas (A_{xy} , A_{xz} , A_{yz}), respectively. Assuming that the average structure of hundreds of foci is isotropic in reality and provided A_{xy} as the standard area, then a Z-correction factor is defined as $F_z = (2A_{xy}) / (A_{xz} + A_{yz})$. The measurement of four experiments, each experiment with more than 200 foci, resulted in a correction factor F_z of 0.39 ± 0.01 (mean \pm SEM) in our study. The final mean focus volume was obtained by the measured volume multiplied by F_z . (Note that individual foci should have different correction factors due to their different size.)

The FociPicker3D Focus Analysis Algorithm

Traditional particle/focus counting programs first set an intensity threshold to convert the image to a binary image and then segment the binary image to a mask image containing separated objects that are then counted as the number of the foci. This method cannot efficiently discriminate the densely distributed objects due to object overlapping and a large intensity variance. To circumvent these limitations we developed a FociPicker3D plug-in for the public image processing software ImageJ (20). This plug-in is capable of discriminating the densely distributed/contacting immunofluorescent foci in 2D and 3D images and then measures the volume, area, intensity and coordinates of these recognized foci.

Figure 2 illustrates the main principle and the workflow of the FociPicker3D algorithm. Figure 2A presents the 1D intensity profile of a focus streak. The algorithm first searches for local maxima. The i th maximum consists of one pixel or a group of connected pixels possessing the same largest value (peak height H_i) in its surrounding pixels. Then a constant fraction F (0–100%) is used to define the local threshold $T_i = F \cdot H_i$ for the i th maximum. The algorithm determines the border of the i th focus at the pixel that is equal to its local threshold T_i , or determines the border at the minimum between two maxima (if the minimum is larger than the local threshold T_i). By changing F , areas of different brightness in the foci can be analyzed without changing the results of focus recognition. For example, using a fraction F of 50% will analyze only the object pixels that are brighter than the half of its maximum brightness. In addition, for images with high background levels, the algorithm calculates the background of the i th maximum (B_i) using its surrounding pixels within a given radius r . In this case, the peak height H_i is defined as $H_i = H_i' - B_i$, and T_i is defined as $T_i = F \cdot H_i + B_i$, where H_i' is the absolute brightness including the background level.

Compared to the 1D illustration of the object segmentation shown in Fig. 2A, the object segmentation in 3D space is much more complex. The FociPicker3D defines that: (1) an object consists of a

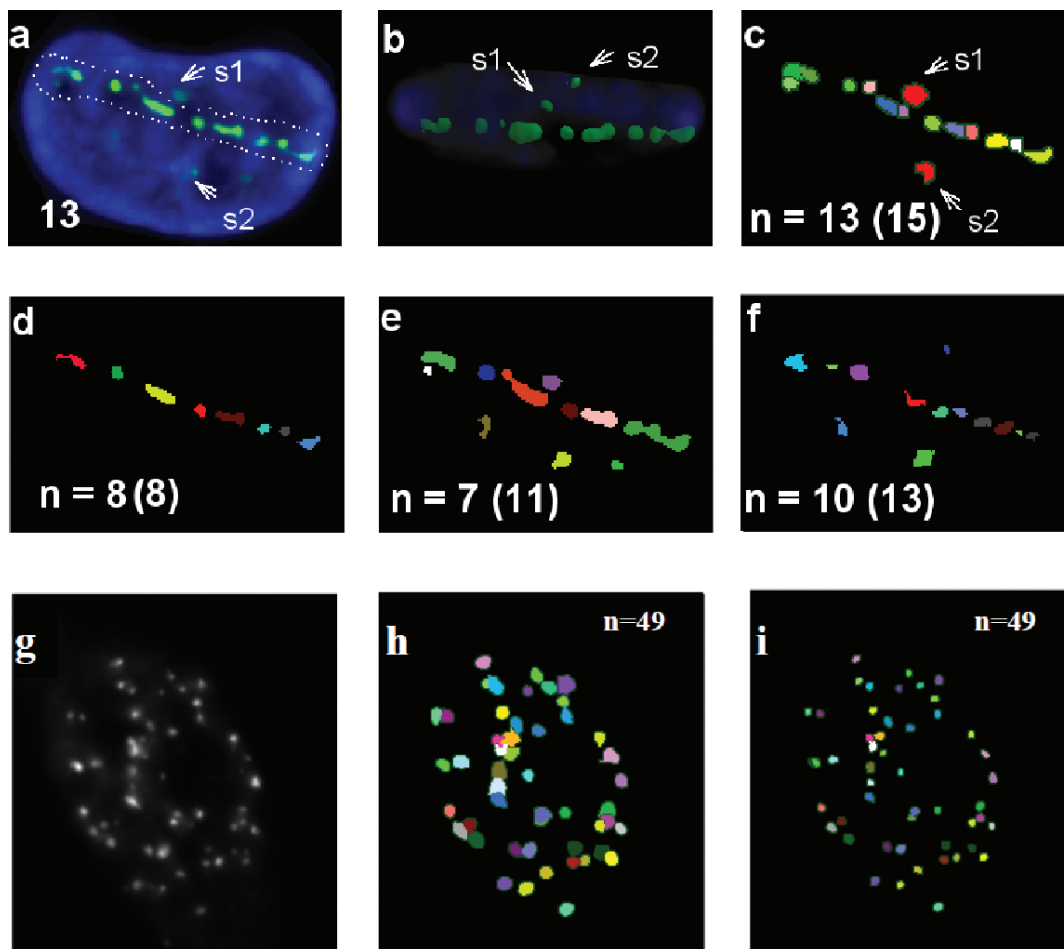


FIG. 3. Focus discrimination using the FociPicker3D algorithm and the thresholding methods. Panel a: An immunofluorescence microscope image showing 53BP1 foci (green) densely distributed along the carbon-ion trajectory in BJ1-hTERT cell nucleus (blue) 3 min after small-angle irradiation. Panel b: Side view of the 3D illustration of the same cell (foci in green and nucleus in gray blue). Panel c: The mask of recognized foci using the FociPicker3D (20% fraction threshold). Panels d–f: Mask of recognized foci using the thresholding method with high threshold setting (d), low threshold setting (e) and its combination with the 3D top-hat transformation (f). Panels a, c–f are projections of the corresponding image/mask stacks. The spontaneous foci s1 and s2 are indicated by the arrows in panels a–c. The numbers of recognized foci in the streak ROI and the whole cell nucleus (numbers in parentheses) are shown. Panels g–i: Discrimination of γ -H2AX foci in HeLa cells irradiated with 1 Gy of X rays using the FociPicker3D algorithm. Panel g: Fluorescence image of a HeLa cell nucleus immunostained with γ -H2AX antibody; the cell was fixed at 45 min after irradiation. Panels h and i: Focus masks generated by FociPicker3D with 20% fraction threshold (h) and 50% fraction threshold (i). The two fraction thresholds result in the same number of foci. The minimum volume of foci used in the focus discrimination is $0.02 \mu\text{m}^3$. All images are presented as the max-projection of the corresponding image stacks.

collection of connected pixel coordinates; (2) the pixel coordinates are stored descendingly (according to their pixel value) in the collection; (3) every registered pixel with mask value i in the i th collection possesses no unregistered neighbor pixels in its $3 \times 3 \times 3$ surrounding voxel in the mask image (this is called closeness validation). First, a 3D mask image is generated for the registration of the pixel coordinates in the recognized foci. All the mask pixels are initialized to a value of zero that represents unregistered pixels. Then the pixels belonging to the object i will be reassigned with value i , and the object border will be registered as “border pixels” in the mask image. For the i th maximum with local threshold T_i , the workflow of the object discrimination is shown in Fig. 2B. Finally, measurements of volume, area, mean intensity and intensity-weighted center are performed on the mask pixels in the object. The measurement determines whether the recognized object i qualifies for the validation of minimum volume and/or intensity variance settings. If not, the object i is

removed from the result. Finally, the result of the qualified objects (foci) is output into an Excel™ table. At the same time, the object mask image is shown in color for control of the focus recognition (see the typical mask image in Fig. 3c).

Biophysical Simulation Calculations

The biophysical code PARTRAC (21) and its recently developed module for DNA repair (15) were used for supplementary simulation calculations mimicking the experimental system. DSB induction was calculated for 1000 carbon ions with an initial energy of 55 MeV traversing the central region of a fibroblast nucleus at an angle of 75° toward the z axis. Calculation methods are described in ref. (21) and references therein. The spatio-temporal development of DNA ends during repair via non-homologous end joining was calculated for 50 ion tracks with a parameter set from a model adaptation to measured

DNA repair kinetics after nitrogen-ion irradiation (22). The diffusion coefficient used was $0.6 \mu\text{m}^2/\text{h}$ (i.e. $170 \text{ nm}^2/\text{s}$) for free DNA ends (DNA ends before going into synapsis with another DNA end) adopted from the work of Jakob *et al.* (29). After synapsis a 10-fold reduced diffusion coefficient of $0.06 \mu\text{m}^2/\text{h}$ was used for the linked DNA ends with attached DNA-PK at both ends.

RESULTS

Validation of Focus Recognition

We first checked the reliability of the automatic focus counting using the FociPicker3D plug-in. Figure 3a shows a typical image of the focus streak immediately after ion irradiation. The streak consists of bright immunofluorescent foci distributed densely in a line. Figure 3a also shows spontaneous 53BP1 foci (indicated by the arrow s1 and s2) that were not induced by the ion traversal. They are located out of the plane of the ion trajectory (Fig. 3b) with slight differences in intensity and structure from the foci in the streak ROI. In addition, their number agrees with the number of 53BP1 foci generally detected in unirradiated cells, and they are located further apart from the streak than would be expected for breaks resulting from delta rays caused by 55 MeV carbon ions (see the calculated DSB yields as a function of the distance to the ion track in Fig. 7a). Therefore, to obtain the information on foci from the ion radiation-induced foci, ROI selection of the focus streak is necessary, as described in the Materials and Methods section.

Using individual immunofluorescence microscopy images of the focus streaks, we first compared the FociPicker3D to available threshold setting and top-hat filter processing methods for discriminating densely distributed foci. As an example, Fig. 3a–c shows a focus streak containing 13 foci in the ROI as analyzed by FociPicker3D and as counted by eye. The discrimination done by the 3D Object Counter (18) based on the thresholding method could only resolve 7–8 foci ($\sim 40\%$ less) in the streak with either high or low thresholds (Fig. 3d–e). The combination of the top-hat transformation with the thresholding method improved the discrimination but still could not resolve all the foci in the streak due to focus overlapping and intensity inhomogeneity (Fig. 3f). Figure 3g–i shows that the FociPicker3D also obtained a convincing result in discriminating sparsely distributed foci in HeLa cells exposed to X rays. In addition, the fraction-thresholding feature of the FociPicker3D allows analyzing the foci with different brightness settings while obtaining the same number of foci, as demonstrated in Fig. 3h–i.

Using individual immunofluorescence images of focus streaks, the parameter settings of the FociPicker3D were optimized. Then the focus streaks of γ -H2AX, 53BP1 and phospho-NBS1 proteins [for HeLa and BJ1-hTERT cells, respectively, 90 cells co-stained with γ -H2AX and

phospho-NBS1, plus 90 cells stained with γ -H2AX and 90 cells stained with 53BP1 antibody, for a total 270 cells (360 foci images) for each cell line] were analyzed by the FociPicker3D plug-in and compared to manual focus counting. To obtain the accurate number of foci in the 3D slices, manual focus counting was done independently by two persons, and intensity profile plotting was used to distinguish overlapping foci (fewer foci were counted only by eye). As shown in Fig. 4, with the FociPicker3D analysis similar results concerning the number of foci were obtained as with the computer-aided manual counting. Note that although the time-consuming computer-aided manual counting gives the same results for focus numbers as the FociPicker3D plug-in, the manual counting cannot provide further information about the foci, whereas the FociPicker3D plug-in can also determine the volumes, intensities and positions of the recognized foci.

Evolution of Focus Structure

The accumulation of 53BP1 and the phosphorylation of H2AX and NBS1 take place around the site of the DSB after irradiation. Consequently, accumulated/phosphorylated proteins form extended foci that are visible under immunofluorescence microscopy. We examined the development of the focus structure quantitatively by measuring the volume of the foci using FociPicker3D in immunofluorescence images. As shown in Fig. 5a, there is initially an increase in the volume of individual foci of all three proteins. While γ -H2AX foci reach a maximum volume after 15 min, phospho-NBS1 and 53BP1 foci reach their maximum at 45 min after irradiation. The measurement also shows that γ -H2AX foci are larger than the phospho-NBS1 and 53BP1 foci at the beginning. The total focus volume of these proteins in a streak first grows by a factor of ~ 2 – 3 (Fig. 5c); then the volume of γ -H2AX decreases while that of 53BP1 and phospho-NBS1 stays relatively constant from 45 min to 6 h after irradiation.

Focus Density

In contrast to sparsely ionizing radiations, 55 MeV carbon ions produce DSBs only ($>99\%$ probability) in the volume within a radial distance of $0.5 \mu\text{m}$ to the ion trajectory (23). Therefore, it is reasonable to use the focus density (the total number of foci in a focus streak divided by the streak length) instead of the total number of foci for comparison between different cells and experiments. As shown in Fig. 5b, the density of γ -H2AX foci increases from 1.2 to 1.5 foci/ μm within 1 h after irradiation. Phospho-NBS1 and 53BP1 proteins showed slight increases in focus density in the first hour after irradiation. Between 1 and 6 h postirradiation, no significant change was found in the focus density of all three proteins. Compared to 53BP1 and phospho-NBS1 proteins, γ -H2AX showed more foci (0.2–0.4 focus/ μm

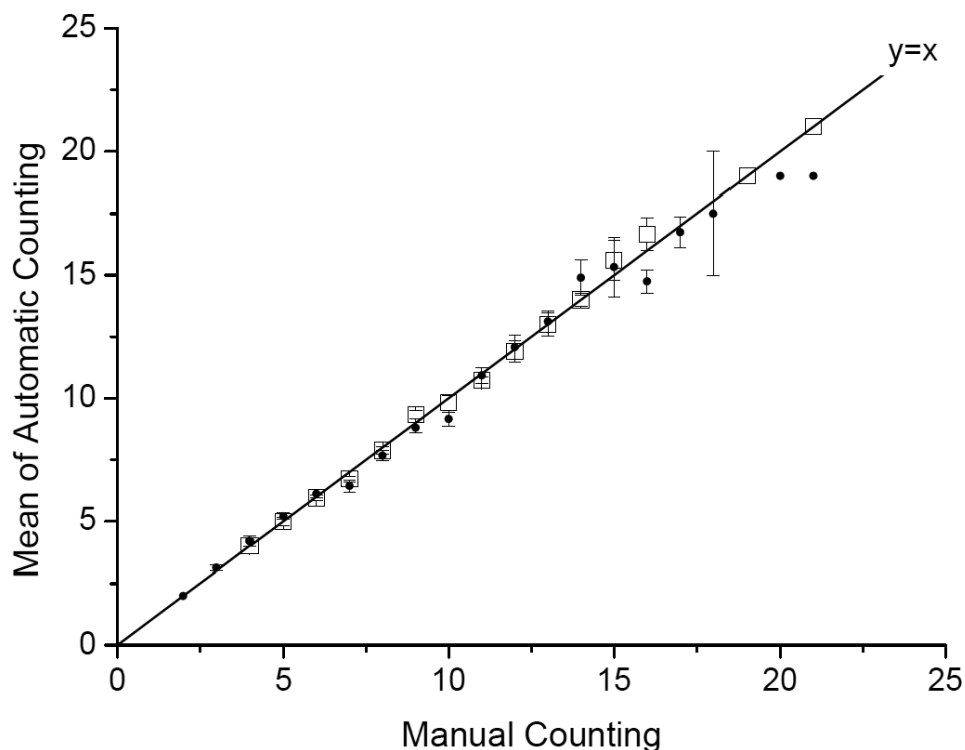


FIG. 4. The focus numbers in BJ1-hTERT (\square) and HeLa cells (\bullet) obtained by automatic counting using the FociPicker3D agrees well with the results of the manual counting. The error bars represent the SEM of the automatic counting. In total 270 cells were evaluated for each cell line. Details are given in the text.

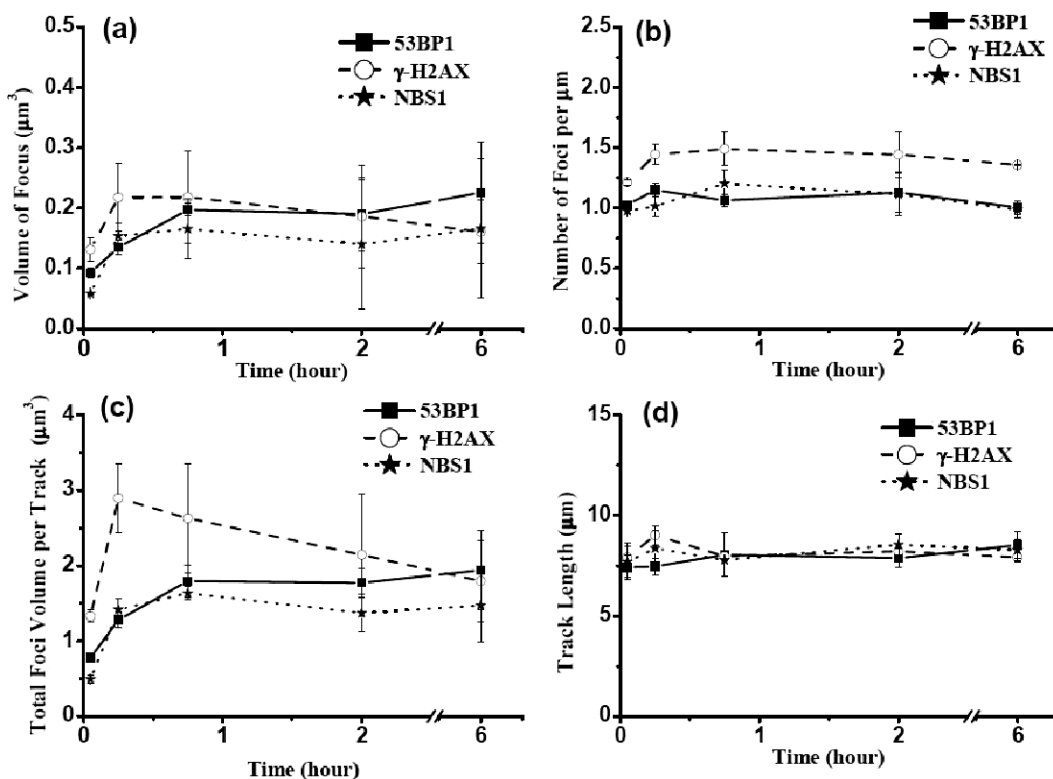


FIG. 5. Alterations of γ -H2AX, 53BP1 and phospho-NBS1 proteins with time relative to the volume of individual foci in BJ1-hTERT cells (panel a), the focus density along the ion trajectory (panel b), the total focus volume in a focus streak (panel c), and the length of the focus streak (panel d). Data are means \pm SEM of two experiments (each data point the sample consists of 30 to 60 cells in each experiment).

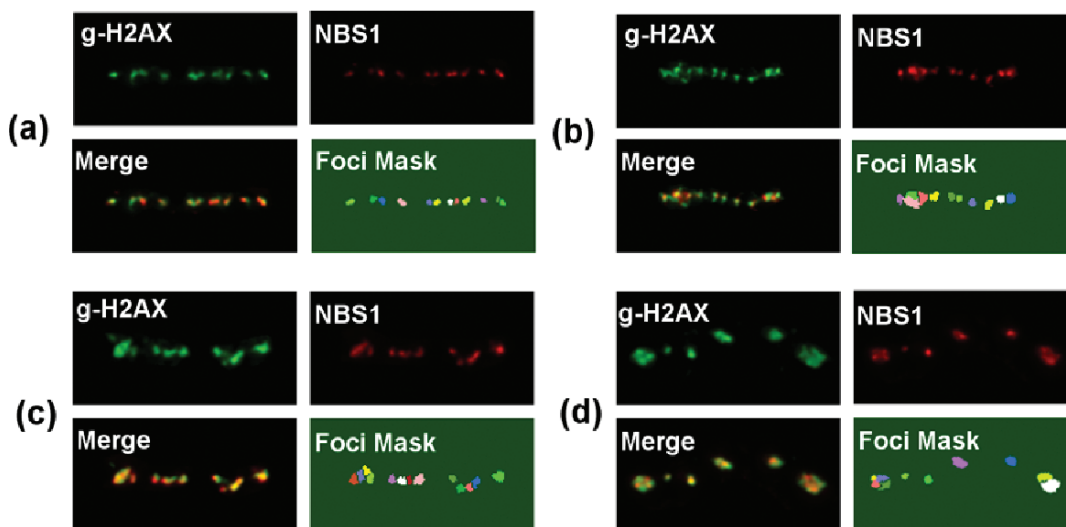


FIG. 6. The morphology of γ -H2AX and phospho-NBS1 focus streaks after 55 MeV carbon-ion irradiation at 3 min (panel a), 15 min (panel b), 45 min (panel c) and 6 h (panel d) postirradiation. The initial linear focus streaks become distorted and large focus clusters are visible at later times. The focus clusters appear as large bright spots containing several local maxima, which were revealed as several foci by the FociPicker3D algorithm (the Foci Mask panels are generated using the phospho-NBS1 streak images). The phospho-NBS1 and γ -H2AX protein colocalize along the streak and also in the cluster regions formed later.

more) in the ion trajectory. No significant difference was found in the length of the focus streak of the different proteins, and the streak length remained constant during 6 h after irradiation (Fig. 5d).

Spatial Dynamics

Immunofluorescence images of the protein focus streak at different times after carbon-ion irradiation are shown in Fig. 6. Immediately after irradiation, all of the foci had a linear distribution resembling the ion trajectory. After longer incubation times, the linear streaks became distorted but were still visible; sparse clusters formed in parts of the focus streaks, and the gap between these foci and clusters became larger (the

clusters are not formed in all focus streaks; a few streaks without clusters also existed at 6 h after irradiation). Using the FociPicker3D, most of these clusters could still be separated into individual foci (see for example the clusters at the left in Fig. 6b–d). These images also demonstrate that γ -H2AX and phospho-NBS1 protein colocalize at the site of DNA damage and that the formation of clusters does not show any visible effects on the colocalization. This colocalization remained for at least 6 h after ion irradiation.

To quantitatively measure the spatial kinetics of the foci relative to the ion trajectory, we determined a virtual trajectory by linear fitting of the focus coordinates in each streak, and then the distances from the foci to the fitted line were measured. As shown in Fig. 7a, immediately

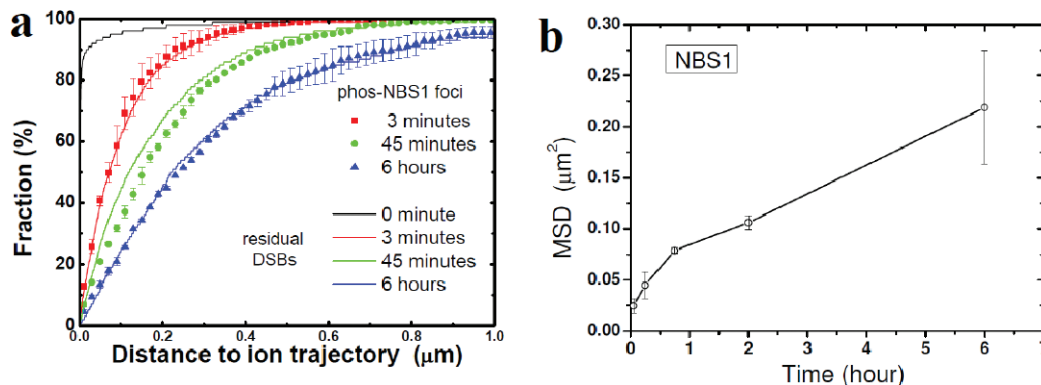


FIG. 7. Panel a: The measured distribution of distances of phospho-NBS1 foci from the trajectory of carbon ions in BJ1-hTERT cells and a corresponding simulated distribution for the residual DSBs using the PARTRAC code. The error bars represent the SEM of two experiments. Panel b: The mean square distance (MSD) of the phospho-NBS1 foci from the ion trajectory. Data are presented as means \pm SEM of two experiments.

after irradiation, 85% of the phospho-NBS1 foci were found around the ion trajectory within a distance of 200 nm, while at 6 h only 40% of the foci were found within this distance due to the distortion of the focus streaks. The spreading curves of γ -H2AX and 53BP1 foci were similar to that of phospho-NBS1 foci (data not shown). Figure 7b shows the mean square distance (MSD) from the phospho-NBS1 foci to the virtual ion trajectory as a function of time t . Considering that for a one-dimensional diffusion, $MSD = 2Dt$, where D is the diffusion coefficient, a decrease in the diffusion coefficient is observed. Assuming that the focus distribution is close to the calculated DSB distribution immediately after irradiation as shown in Fig. 7a, an initial diffusion coefficient of around $0.25 \pm 0.07 \mu\text{m}^2/\text{h}$ (mean \pm SE of two experiments) within 3 min and an average diffusion coefficient of $0.018 \pm 0.005 \mu\text{m}^2/\text{h}$ within 6 h after irradiation were obtained.

Calculated Induction and Rejoining of DSBs

Using the PARTRAC code, we calculated the induction and rejoining of DSBs after carbon-ion irradiation. The simulation calculations yielded a mean number of 144 DSBs along an average track length of 9.6 μm for the 55 MeV carbon ions. The DSBs were spatially clustered in 50 chromatin fiber regions of 5 kbp and distributed over 28 chromatin domains of 1 Mbp. Thus the densities per micrometer track length were 15 DSBs, 5.2 chromatin fiber elements carrying DSBs, and 2.9 such 1-Mbp chromatin domains. Compared to ^{60}Co γ rays, these yields corresponded to RBE values of 2.55 for total DSBs and 0.90 for 5-kbp chromatin fiber elements with DSBs.

The cumulative distributions of the projection along the z axis of the radial distance between the calculated residual DSBs and the ion track are presented in Fig. 7a. Initially, about 95% of the DSBs occurred within a distance of 200 nm from the track. The calculated numbers of still unrejoined DNA ends (each DSB generates two DNA ends) per track after 3 min, 45 min and 6 h repair time were 240, 120 and 34, respectively, and calculated distances from ion tracks were distributed similarly to those for phospho-NBS1 foci.

DISCUSSION

Manual counting of immunofluorescent foci has the advantages of high tolerance and visual checking in focus recognition, but it suffers from low throughput and subjectivity of different examiners. Automatic counting has the advantage of high throughput and capability of obtaining quantitative information (such as focus size, fluorescence intensity and focus position, etc.), but it is also limited by the software availability in laboratories and the reliability/efficiency of focus recognition algorithms. We tested the thresholding and

its combination with 3D top-hat filter to discriminate the densely distributed and overlapping foci along the high-LET carbon-ion trajectory in BJ1-hTERT cells. The top-hat filter processing improved the discrimination of the thresholding method but still could not recognize all foci in the streak (Fig. 3d–f). In contrast, the FociPicker3D algorithm using the local fraction threshold setting not only gives efficient focus discrimination using individual focus images of carbon-ion-irradiated cells and X-irradiated cells but also yields focus-counting results consistent to the computer-aided manual counting method. Thus the FociPicker3D is suitable for analysis of both sparsely and densely distributed foci after exposure to both low-LET and high-LET ionizing radiations.

After a previous report on the kinetics of the individual foci along the trajectory of GeV iron ions using wavelet processing on 2D microscope images (24), we performed 3D high-resolution microscopy to investigate the focus structure in more detail and to facilitate the recognition of overlapping foci. The number density of γ -H2AX foci in BJ1-hTERT cells reached a maximum of 1.5 foci/ μm at 45 min, from 1.2 foci/ μm at 3 min, indicating that 80% of the foci are detected at the earliest time after carbon-ion irradiation that can be assessed by immunofluorescence analysis with our experimental setup (similar results were obtained with irradiated HeLa cells; data not shown). The number density of γ -H2AX foci then showed a slight decrease up to 6 h after irradiation (Fig. 5b). In contrast, in a previous study, Leatherbarrow *et al.* observed that after 1 Gy γ irradiation only 20% foci were visible within 3 min compared to the maximum number measured at 30 min, and the number of γ -H2AX foci decreased significantly in V79-4, HF19 and xrs-5 cells in 2 h (10). The difference shows that the kinetics of γ -H2AX focus disappearance after high-LET carbon-ion irradiation is slower than that after low-LET irradiations. This result is in line with the experiments where the total γ -H2AX intensity was measured after high- and low-LET irradiation (25).

In a previous publication, Jakob *et al.* determined a constant diffusion of IRIF up to 6 h after irradiation with a diffusion coefficient of $0.6 \mu\text{m}^2/\text{h}$ using live cell imaging (29). Here we obtained a comparable diffusion coefficient of $0.25 \pm 0.07 \mu\text{m}^2/\text{h}$ in the first minutes after irradiation, but for later times we observed a much slower (less than a tenth) diffusion behavior of the IRIF (Fig. 7b). This decrease in the diffusion coefficient is in accord with an assumed reduction of the diffusion of DSBs in synapsis. Assuming a tenfold reduction in the PARTRAC model, the simulated residual DSBs show a distribution very close to that of the experimental IRIF (Fig. 7a). The long-term difference in the diffusion coefficient between our measurements and those in ref. (29) may result from an overestimation of the diffusion due to imperfect correction for motion and morphology

changes in the whole nucleus in the work of Jakob *et al.* (30). The linear fitting of the virtual ion trajectory automatically compensates for the motion and morphology changes in the cell nucleus. It could, however, underestimate the distance of the foci from the fitted ion track (i.e. the diffusion), especially when there are few foci in the ion track.

Clusters containing several foci were first found at 15 min postirradiation (very few) and more clusters were found in the focus streak at later times, but none were found at 3 min after carbon-ion irradiation. Individual foci (local maxima) were discriminated in the clusters (Fig. 6) using FociPicker3D, and in the cluster-formed streaks there were typically large spaces between foci and clusters (Fig. 6). The immunofluorescence images showed that phospho-NBS1 and γ -H2AX proteins colocalize in the foci formed along the ion trajectory immediately after irradiation. This observation is in accordance with previous studies demonstrating that phosphorylated NBS1 binds to γ -H2AX at the DNA damage site (26, 27). This colocalization of phospho-NBS1, γ -H2AX and 53BP1 (data not shown) remains stable in the formed focus clusters for 6 h postirradiation (Fig. 6), indicating that the newly visible foci represent sites of DSB damage.

The observation of focus clusters is in accordance with previous reports that focus clusters were observed in cells traversed by α particles (14). Krawczyk and his coworkers interpreted these clusters as being formed by aggregation of neighboring foci (28). However, using live cell imaging, Jakob *et al.* observed that there was no general tendency to form focus clusters in the cells irradiated with high-LET ions (29). Based on our work, we propose the following model for the formation of the focus clusters: Along the ion trajectory DSBs and DSB clusters at some specific site are produced by the densely ionizing radiation of carbon ions. Immediately after irradiation, both individual DSBs and individual DSB clusters are revealed as individual foci under immunofluorescence microscopy using conventional wide-field or confocal microscopes with optical resolution of >200 nm. Later, some foci disappear because of DSB repair, resulting in the growing gap in the focus streak. At the same time, in concert with the diffusion of the DSB ends in the DSB clusters, some DSBs (i.e. new foci) become visible in the vicinity of the DSB clusters, resulting in the formation of focus clusters. This model is supported by the following observations in our experiments: (1) the agreement of the experimental spread of the foci and the simulated spread of the residual DSB ends (Fig. 7a); (2) the fact that fewer foci are detected than the calculated DSB number; (3) the disappearance of foci due to repair and appearance of foci due to DSB diffusion, which may result in the relatively constant kinetics of γ -H2AX foci; and (4) the focus volume increases within 45 min after irradiation, which may

indicate the diffusion of DSBs (foci) from the DSB clusters, in addition to the protein diffusion at the focus site.

Jakob *et al.* reported that irradiations with bismuth ions of much higher LET (13,600 keV/ μ m) produce a similar focus pattern along the ion trajectory as carbon ions (LET around 300 keV/ μ m) (13). Here, according to our calculations using PARTRAC, merging of all DSBs within the same spherical chromatin domain (1 Mbp in a sphere about 0.5 μ m in diameter) or even a small number of such domains does not reduce the density of DSBs to the observed number of foci per μ m track length [see also ref. (23)]. Therefore, the discrepancy between visible foci and calculated DSBs for high-LET radiations suggests that some of these DSBs are not detected through immunofluorescence microscopy, which is limited by the optical resolution of wide-field and confocal microscopy or the immunostaining technique. Recently, a series of novel super-resolution microscopy techniques have been developed that can reach an optical resolution of tens of nanometers (30). The application of one of these novel microscopes, localization microscopy (31), to resolving the fine structure of the protein foci in our group is now in progress.

ACKNOWLEDGMENTS

This work has been supported by the DFG Cluster of Excellence, Munich-Centre for Advanced Photonics, CAS project Y150310BR0, BfS project StSch 4450, as well as the Maier Leibnitz Laboratorium of the Ludwig-Maximilians-Universität München and the Technische Universität München. The authors claim no conflict of interest. The FociPicker3D is an open-source plug-in of ImageJ developed for focus analysis using 2D and 3D microscope images (32).

Received: February 11, 2011; accepted: June 28, 2011; published online: July 28, 2011

REFERENCES

1. Rogakou EP, Pilch DR, Orr AH, Ivanova VS, Bonner WM. DNA double-stranded breaks induce histone H2AX phosphorylation on serine 139. *J Biol Chem* 1998; 273:5858–68.
2. Paull TT, Rogakou EP, Yamazaki V, Kirchgessner CU, Gellert M, Bonner WM. A critical role for histone H2AX in recruitment of repair factors to nuclear foci after DNA damage. *Curr Biol* 2000; 10:886–95.
3. Schultz LB, Chehab NH, Malikzay A, Halazonetis TD. P53 binding protein 1 (53BP1) is an early participant in the cellular response to DNA double-strand breaks. *J Cell Biol* 2000; 151:1381–90.
4. Ward IM, Minn K, Jorda KG, Chen J. Accumulation of checkpoint protein 53BP1 at DNA breaks involves its binding to phosphorylated histone H2AX. *J Biol Chem* 2003; 278:19579–82.
5. Rothkamm K, Löbrich M. Evidence for a lack of DNA double-strand break repair in human cells exposed to very low x-ray doses. *Proc Natl Acad Sci U S A* 2003; 100:5057–62.
6. Löbrich M, Shibata A, Beucher A, Fisher A, Ensminger M, Goodarzi AA, et al. Gamma-H2AX foci analysis for monitoring DNA double-strand break repair: strengths, limitations and optimization. *Cell Cycle* 2010; 9:662–9.

7. Taucher-Scholz G, Jakob B. Ion irradiation as a tool to reveal the spatiotemporal dynamics of DNA damage response processes. In: *Genome integrity*. Heidelberg (Germany): Springer; 2007. p. 453–78.
8. Karlsson KH, Stenerlöv B. Focus formation of DNA repair proteins in normal and repair-deficient cells irradiated with high-LET ions. *Radiat Res* 2004; 161:517–27.
9. Jakob B, Rudolph JH, Gueven N, Lavin MF, Taucher-Scholz G. Live cell imaging of heavy ion induced radiation responses by beamline microscopy. *Radiat Res* 2005; 163:681–90.
10. Leatherbarrow EL, Harper JV, Cucinotta FA, O'Neill P. Induction and quantification of γ -H2AX foci following low and high LET-irradiation. *Int J Radiat Biol* 2006; 82:111–8.
11. Costes SV, Boissière A, Ravani S, Romano R, Parvin B, Barcellos-Hoff MH. Imaging features that discriminate between foci induced by high- and low-LET radiation in human fibroblasts. *Radiat Res* 2006; 165:505–15.
12. Hable V, Greubel C, Bergmaier A, Reichart P, Hauptner A, Krücken R, et al. The live cell irradiation and observation setup at SNAKE. *Nucl Instrum Methods B* 2009; 267:2090–7.
13. Jakob B, Scholz M, Taucher-Scholz G. Biological imaging of heavy charged particle tracks. *Radiat Res* 2003; 159:676–84.
14. Aten JA, Stap J, Krawczyk PM, van Oven CH, Hoebe RA, Essers J, et al. Dynamics of DNA double-strand breaks revealed by clustering of damaged chromosome domains. *Science* 2004; 303:92–5.
15. Friedland W, Jacob P, Kundrat P. Stochastic simulation of DNA double-strand break repair by non-homologous end joining based on track structure calculations. *Radiat Res* 2010; 173:677–88.
16. Dollinger G, Hable V, Hauptner A, Krücken R, Reichart P, Friedl AA, et al. Microirradiation of cells with energetic heavy ions. *Nucl Instrum Methods B* 2005; 231:195–201.
17. Greubel C, Hable V, Drexler GA, Hauptner A, Dietzel S, Strickfaden H, et al. Competition effect in DNA damage response. *Radiat Environ Biophys* 2008; 47:423–9.
18. Bolte S, Cordelières FP. A guided tour into subcellular colocalization analysis in light microscopy. *J Microscopy* 2006; 224:213–32.
19. TopHatFilter3D. Available from: <http://u759.curie.u-psud.fr/software/u759.html>.
20. Rasband WS. ImageJ. Bethesda (MD): NIH, 1997–2010. Available from: <http://rsb.info.nih.gov/ij/>.
21. Friedland W, Dingfelder M, Kundrát, P, Jacob P. Track structures, DNA targets and radiation effects in the biophysical simulation code PARTRAC. *Mutat Res* 2011; 711:28–40.
22. Stenerlöv B, Höglund E, Carlsson J, Blomquist E. Rejoining of DNA fragments produced by radiations of different linear energy transfer. *Int J Radiat Biol* 2000; 76:549–57.
23. Hauptner A, Friedland W, Dietzel S, Drexler GA, Greubel C, Hable V, et al. Spatial Distribution of DNA double-strand breaks from ion tracks. *Matematisk-fysiske Meddelelser* 2006; 52:59–85.
24. Costes SV, Ponomarev A, Chen JL, Nguyen D, Cucinotta FA, Barcellos-Hoff MH. Image-based modeling reveals dynamic redistribution of DNA damage into nuclear sub-domains. *PLoS Comput Biol* 2007; 3:e155.
25. Schmid TE, Dollinger G, Beisker W, Hable V, Greubel C, Auer S, et al. Differences in the kinetics of gamma-H2AX fluorescence decay after exposure to low and high LET radiation. *Int J Radiat Biol* 2010; 86:682–91.
26. Furuta T, Takemura H, Liao ZY, Aune GJ, Redon C, Sedelnikova OA, et al. Phosphorylation of histone H2AX and activation of Mre11, Rad50, and Nbs1 in response to replication-dependent DNA double-strand breaks induced by mammalian DNA topoisomerase I cleavage complexes. *J Biol Chem* 2003; 278:20303–12.
27. Kobayashi J. Molecular mechanism of the recruitment of NBS1/hMRE11/hRAD50 complex to DNA double-strand breaks: NBS1 binds to gamma-H2AX through FHA/BRCT domain. *J Radiat Res* 2004; 45:473–8.
28. Krawczyk PM, Stap J, van Oven C, Hoebe R, Aten JA. Clustering of double strand break-containing chromosome domains is not inhibited by inactivation of major repair proteins. *Radiat Prot Dosimetry* 2006; 122(1–4), :150–3.
29. Jakob B, Splinter J, Durante M, Taucher-Scholz G. Live cell microscopy analysis of radiation-induced DNA double-strand break motion. *Proc Natl Acad Sci U S A* 2009; 106:3172–7.
30. Hell SW. Microscopy and its focal switch. *Nat Methods* 2009; 6:24–32.
31. Gunkel M, Erdel F, Rippe K, Lemmer P, Kaufmann K, Hoermann C, et al. Dual color localization microscopy of cellular nanostructures. *Biotechnol J* 2009; 4:927–38.
32. Du G. FociPicker3D [internet: cited 2011 Feb 10]. Available from: <http://rsbweb.nih.gov/ij/plugins/foci-picker3d/>.